Optical Materials 174 (2026) 117903

Contents lists available at ScienceDirect

Optical Materials

journal homepage: www.elsevier.com/locate/optmat

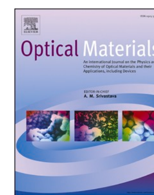

Research Article

Composition-dependent optical properties and dielectric function modeling of PECVD-grown hydrogenated amorphous silicon carbonitride thin films

Y. Vygranenko [a,*], G. Lavareda [a,b,c], A. Amaral [c,d], P. Brogueira [c,d]

[a] CTS/LASI, Faculdade de Ciências e Tecnologia, Universidade Nova de Lisboa, Campus da Caparica, 2829-516, Caparica, Portugal
[b] Departamento de Ciência dos Materiais, Faculdade de Ciências e Tecnologia, Universidade Nova de Lisboa, Campus da Caparica, 2829-516, Caparica, Portugal
[c] CeFEMA/LaPMET, Instituto Superior Técnico, Universidade de Lisboa, Av. Rovisco Pais 1, 1049-001, Lisboa, Portugal
[d] Departamento de Física, Instituto Superior Técnico, Universidade de Lisboa, Av. Rovisco Pais 1, 1049-001, Lisboa, Portugal

ARTICLE INFO

Keywords:
A-SiCN:H thin films
rf-PECVD
Dielectric function
Extended Tauc–Lorentz model
Optical bandgap
Refractive index dispersion

ABSTRACT

Hydrogenated amorphous silicon carbonitride (a-SiCN:H) thin films were deposited by radio-frequency plasma-enhanced chemical vapor deposition (rf-PECVD) at 150 °C using SiH_4, CH_4, and NH_3 gas mixtures with variable flow ratios. The chemical composition and hydrogen content, determined by Rutherford backscattering and elastic recoil detection analyses, revealed Si-rich carbonitrides containing 32–52 at.% Si, 3–5 at.% C, 16–44 at.% N, and 25–30 at.% H. Atomic force microscopy confirmed smooth and uniform film surfaces with RMS roughness below 1 nm, suitable for precise optical modeling. Optical transmission spectra were analyzed using an extended Tauc–Lorentz (XTL) dispersion model capable of describing non-exponential band-tail absorption. The XTL model provided excellent agreement with experiment and allowed extraction of the real and imaginary parts of the dielectric function, including sub-gap components. The optical bandgap, derived from Tauc plots, increased linearly with the elemental N/Si ratio, reflecting enhanced Si–N bond formation and a reduction in localized electronic states. The refractive index varied between 1.77 and 2.9, showing strong dependence on composition and photon energy. These results demonstrate that rf-PECVD enables low-temperature synthesis of uniform a-SiCN:H films with controllable optical properties, suitable for optoelectronic and photonic device applications.

1. Introduction

Hydrogenated amorphous silicon carbonitride (a-SiCN:H) thin films are of great interest in optoelectronics and photovoltaics due to their excellent mechanical properties [1,2], chemical inertness [3,4], and tunable optical characteristics [5–7]. These films are ideal for applications such as antireflection coatings in Si-based solar cells [8], silicon optical components [9], and optical interference filters [10]. Additionally, a-SiCN:H is a promising low-loss material for photonic integrated circuits, offering functionality across a wide spectral range, from visible (VIS) for biophotonics to the near-infrared (NIR) for telecommunications, and extending into the mid-infrared (MIR) for spectroscopic applications [11]. As a Group-IV semiconductor compound, a-SiCN:H exhibits intense optical nonlinearity, making it a key candidate for high-speed photonic devices with all-optical switching [12].

A variety of physical and chemical vapor deposition techniques have been employed for the synthesis of amorphous and nanocomposite silicon carbonitride thin films, each offering distinct advantages in terms of film quality, microstructure, and process control. Magnetron sputtering is widely used due to its excellent uniformity and strong adhesion, enabling dense SiCN coatings with controlled stoichiometry through co-sputtering or reactive sputtering from Si, graphite, SiN, or SiC targets [6,13–15]. Pulsed laser deposition (PLD) has been applied to produce SiCN films with high purity and smooth interfaces, benefiting from precise control over film thickness and stoichiometry, though limited in scalability [16]. Ion beam-assisted deposition (IBAD) and ion beam sputtering (IBS) techniques allow for additional energy control at the substrate, improving film densification and hardness [17]. Low-pressure chemical vapor deposition (LPCVD) is capable of producing high-quality SiCN films with excellent thermal stability, but typically requires substrate temperatures above 700 °C, limiting their compatibility with thermally sensitive materials [18]. In contrast, hot-wire CVD (HWCVD) enables lower-temperature deposition (often 100–400 °C) of high-quality SiCN films with good thermal stability, improving compatibility with thermally sensitive materials [19,20]. Radio-frequency plasma-enhanced chemical vapor deposition

* Corresponding author.
E-mail address: yvygranenko@deetc.isel.ipl.pt (Y. Vygranenko).

https://doi.org/10.1016/j.optmat.2026.117903
Received 3 November 2025; Received in revised form 2 January 2026; Accepted 19 January 2026
Available online 20 January 2026
0925-3467/© 2026 The Authors. Published by Elsevier B.V. This is an open access article under the CC BY-NC-ND license (http://creativecommons.org/licenses/by-nc-nd/4.0/).

(rf-PECVD) enables low-temperature (<400 °C) growth with precise control over composition and hydrogen incorporation through the adjustment of precursor gas ratios and plasma parameters [2,5–7]. The versatility, uniformity, and scalability of rf-PECVD make it the most suitable technique for tailoring SiCN thin films across a wide compositional and functional range [10,21].

The optical constants of a-SiCN:H thin films are strongly dependent on their elemental composition, which can be continuously tuned from Si-rich to C-rich and N-rich regimes by adjusting the deposition conditions. It has been shown that increasing nitrogen incorporation leads to a widening of the optical band gap accompanied by a reduction in the refractive index, whereas higher silicon or carbon contents result in narrower band gaps and increased refractive indices, reflecting composition-dependent changes in bonding configuration and amorphous network structure [7]. The influence of precursor chemistry in PECVD-grown films has been demonstrated through comparative studies employing methane and acetylene hydrocarbon sources, which revealed that variations in carbon incorporation, hydrogen content, and film density significantly affect both the refractive index and optical band gap [22]. Similar correlations between optical band gap and refractive index have also been reported for a-SiCN:H films deposited from alternative PECVD precursors, confirming the generality of these composition-driven relationships across different synthesis routes [10].

The precise determination of optical constants of a-SiCN:H is crucial for its various applications. Accurate characterization of this material can be achieved using the inverse synthesis method, which fits parametric models to spectroscopic or ellipsometry data. This method requires a Kramers–Kronig consistent model that captures all absorption features within the measured spectral range. Existing models for amorphous materials account for the sub-gap region, where the absorption coefficient increases exponentially (Urbach tail) [23,24]. However, a non-exponential band tail, a feature observed in a-$Si_{1-x}N_x$:H alloy [25], may also apply to a-SiCN:H. To address this, we recently introduced an extended Tauc–Lorentz (XTL) dispersion model, specifically designed for amorphous materials with non-exponential band tails [26]. In this study, we applied a modified version of this model to a-SiCN:H thin films, achieving high precision in determining their optical dielectric functions and providing detailed insights into their absorption features near the band edge.

In this work, hydrogenated amorphous silicon carbonitride (a-SiCN:H) thin films were deposited by rf-PECVD at 150 °C using SiH_4, CH_4, NH_3, and H_2 precursor gases. The film composition was systematically controlled by varying the precursor gas flow ratios, enabling precise adjustment of carbon and nitrogen incorporation. The elemental composition of the films was determined using ion-beam analytical techniques, while surface morphology was examined by atomic force microscopy (AFM), and optical transmission spectra were measured in the UV–Vis–NIR range.

A detailed description of the extended Tauc–Lorentz dispersion model and its implementation for nonlinear least-squares fitting of experimental transmittance data is presented. The model shows excellent agreement with the measured spectra of the a-SiCN:H films, accurately capturing the extended absorption tail below the fundamental absorption edge. The study first examines the compositional and morphological properties of the films, followed by analysis of the dielectric function derived from the fitted model. Finally, correlations among the optical bandgap, optical constants, and elemental composition are established, demonstrating the compositional tunability of rf-PECVD-grown a-SiCN:H thin films and their potential for optoelectronic and photonic applications.

2. Experimental

Thin films were deposited on fused silica substrates using a capacitively coupled, parallel-plate 13.56 MHz PECVD system at a substrate temperature of 150 °C. Prior to deposition, the substrates were cleaned by washing with deionized water and a nonionic detergent, followed by sequential immersion in acetone and isopropanol to remove organic contaminants.

The gases used for thin-film deposition were SiH_4 (Air Liquide, 99.999 % purity), CH_4 (Praxair, 99.995 % purity), NH_3 (Praxair, 99.999 % purity) and H_2 (Air Liquide, 99.999 % purity). A SiH_4/H_2 dilution ratio of 1:9 was employed to prevent silicon polymer deposition on the chamber walls. To maintain a constant residence time of plasma species, the total gas flow rate was kept constantat at 43 ± 0.2 sccm. The process pressure and rf-power were set to 135 Pa and 30W (135 mW/cm^2), respectively. Under constant pressure, maintaining a constant total flow necessarily requires simultaneous adjustment of the individual gas flow rates.

Rutherford Backscattering (RBS), Elastic Backscattering Spectrometry (EBS), and Elastic Recoil Detection Analysis (ERDA) were used to determine the concentrations of the elements in the films. The film thickness was measured by a Veeco Dektak[3] profilometer. AFM measurements were performed by a Dimension 3100 SPM with a Nanoscope IIIa controller from Digital Instruments, in tapping mode, under ambient conditions. Commercial tapping mode etched silicon probes were from Bruker. Optical transmission spectra were measured by a Shimadzu 3100 UV–Vis–NIR spectrophotometer.

3. Extended Tauc–Lorentz model and spectral fitting procedure

In the modified XTL model, the imaginary part of the dielectric function is a piecewise function with two components:

$$\varepsilon_{2,X}(E) = \frac{\varepsilon_{2,TL}(E_c)E}{E_c}\exp\left(p_n\left(\frac{E-E_c}{E_c}\right)\right) \text{at } E < E_c\,, \tag{1a}$$

$$\varepsilon_{2,TL}(E) = \frac{(E-E_g)^2 A E_0 C}{\left(E^2-E_0^2\right)^2 + C^2E^2}\cdot\frac{1}{E} \text{ at } E \geq E_c, \tag{1b}$$

where E_c is the connection energy between the components, and $p_n\left(\frac{E-E_c}{E_c}\right) = b_0 + b_1x + b_2x^2 + \ldots + b_nx^n$, $x = \frac{E-E_c}{E_c}$, is the polynomial term. This formulation differs from the original XTL model [26], in which the polynomial was expressed directly as $p_n(E)$. By normalizing the argument to the dimensionless variable $x = \frac{E-E_c}{E_c}$, coefficients b_n also become dimensionless. In practice, this transformation reduces the dynamic range of the polynomial coefficients, typically confining their absolute values to the range of 1–100. This simplifies the parameter constraints and improves numerical stability during fitting.

To ensure continuity of the function and its first derivative at $E = E_c$, the first two polynomial coefficients are defined as follows: $b_0 = 0$ and

$$b_1 = \frac{2E_g}{E_c - E_g} - \frac{2{E_c}^2\left(C^2 - 2E_0^2 + 2{E_c}^2\right)}{\left({E_c}^2 - E_0^2\right)^2 + C^2{E_c}^2}. \tag{2}$$

By introducing a decoupled band-edge absorption component of the dielectric function

$$\varepsilon_{2,sg}(E) = \begin{cases} \varepsilon_{2,X}(E) & \text{at } E \leq E_g \\ \varepsilon_{2,X}(E) - \varepsilon_{2,TL}(E) & \text{at } E_g < E \leq E_c\,, \\ 0 & \text{at } E > E_c \end{cases} \tag{3}$$

the imaginary part of the dielectric function is expressed as a sum of two components:

$$\varepsilon_2(E) = \varepsilon_{2,TL}(E) + \varepsilon_{2,sg}(E). \tag{4}$$

The real part of the dielectric function is obtained using the Kramers-Kronig integral of Eq. (4):

$$\varepsilon_1(E) = \varepsilon_\infty + \frac{2}{\pi}P\int_{E_g}^{\infty}\frac{\xi\varepsilon_{2,TL}(\xi)}{\xi^2 - E^2}d\xi + \frac{2}{\pi}P\int_0^{E_c}\frac{\xi\varepsilon_{2,sg}(\xi)}{\xi^2 - E^2}d\xi, \tag{5}$$

where ε_∞ represents the value of real part of the dielectric function at infinite energy. The first and second terms in Eq. (5) correspond to the TL model component, $\varepsilon_{1,TL}$, for which an analytical integration is known [27]. The third term, $\varepsilon_{1,sg}$, can be calculated numerically using various methods. We used Maclaurin's formula because of its calculation simplicity and good accuracy [28].

Finally, the XTL model dielectric function is given by:

$$\widetilde{\varepsilon}_{XTL}(E) = \widetilde{\varepsilon}_{TL}(E; A, E_0, E_g, C, \varepsilon_\infty) + \widetilde{\varepsilon}_{sg}(E; E_c, b_1, b_2, \ldots, b_n), \tag{6}$$

where the terms $\widetilde{\varepsilon}_{TL}(E) = \varepsilon_{1,TL}(E) + i\varepsilon_{2,TL}(E)$ and $\widetilde{\varepsilon}_{sg}(E) = \varepsilon_{1,sg}(E) + i\varepsilon_{2,sg}(E)$ are associated with interband and sub-gap optical transitions, respectively. Therefore, the model has (5 + n) parameters to fit, excluding the coefficient b_1, which is defined by Eq. (3). An important advantage of this formulation is its flexible parameterization: the number of adjustable parameters adapts to the complexity of the sub-gap absorption and to the precision of the experimental data. At n = 1, the model reduces to the Tauc-Lorentz-Urbach parameterization, where the absorption coefficient varies exponentially with energy at $E \leq E_c$ [23].

To simulate the experimental transmission spectra, we employed a mathematical model describing the normal-incidence transmittance of a thin film on a transparent substrate. The model accounts for multiple reflections in the substrate, and the total transmittance is given by Ref. [29]:

$$T_{calc} = \frac{T_f T_s}{1 - R_b R_s}, \tag{7a}$$

$$T_s = \frac{4 n_s n_a}{(n_s + n_a)^2}, \tag{7b}$$

$$R_s = \frac{(n_s - n_a)^2}{(n_s + n_a)^2}, \tag{7c}$$

where T_f is the transmittance of the film on the semi-infinite substrate, T_s is the transmittance of the substrate-air interface, R_b is the reflectance at the substrate-film interface, and n_s and n_a are the refractive indices of the substrate and air, respectively. Terms T_f and R_b can be calculated as [30].

$$T_f = \frac{n_s}{n_a} \left| \frac{\frac{2n_a}{n_a + \widetilde{n}_f} \frac{2\widetilde{n}}{n_s + \widetilde{n}_f} e^{i\beta}}{1 + \frac{n_a - \widetilde{n}_f}{n_a + \widetilde{n}_f} \frac{\widetilde{n}_f - n_s}{n_s + \widetilde{n}_f} e^{2i\beta}} \right|^2, \tag{8}$$

$$R_b = \left| \frac{\frac{n_s - \widetilde{n}_f}{n_s + \widetilde{n}_f} + \frac{\widetilde{n}_f - n_a}{\widetilde{n}_f + n_a} e^{2i\beta}}{1 + \frac{n_s - \widetilde{n}_f}{n_s + \widetilde{n}_f} \frac{\widetilde{n}_f - n_a}{\widetilde{n}_f + n_a} e^{2i\beta}} \right|^2, \tag{9}$$

$$\beta = \frac{2\pi d \widetilde{n}_f}{\lambda}, \tag{10}$$

where d is the film thickness, and λ is the wavelength. The complex refractive index of the film, $\widetilde{n}_f = n_f + ik_f$, is derived from Eq. (6) as $\widetilde{n}_f = \sqrt{\widetilde{\varepsilon}_{XTL}}$.

The model parameters are determined by fitting the experimental transmittance data through numerical minimization of an error function. We have developed a C# fitting program implementing the Levenberg–Marquardt algorithm for non-linear least-squares optimization. The algorithm minimizes the weighted residual, defined as:

$$Residue = \frac{1}{M} \sum_{i=1}^{M} \left[\frac{T_i^{meas} - T_i^{calc}}{T_i^{meas} + \sigma(\lambda_i)} \right]^2, \tag{11}$$

where T_i^{meas} is the measured transmittance at wavelength λ_i, and $\sigma(\lambda_i)$ is the measurement accuracy (standard deviation) of the spectrometer, which may depend on λ_i. The denominator $(T_i^{meas} + \sigma(\lambda_i))$ acts as a dynamic weighting factor. When T_i^{meas} is small (strong absorption), $\sigma(\lambda_i)$ prevents overweighting of noisy low-T data. When T_i^{meas} is large, the term behaves as a relative residual.

The fitting procedure includes the following steps: (i) initializing the TL model parameters with physically reasonable values and defining their constraints; (ii) performing an initial fit with a first-order polynomial to fit the transmittance data across the entire measured range; and (iii) iteratively refining the fit with updated parameters by increasing the polynomial order until the fitting accuracy is limited by the spectral noise and/or the precision of the measured data. In most practical cases, the polynomial order does not exceed four.

4. Results and discussion

4.1. Elemental composition and surface topography analysis

Fig. 1 presents the elemental composition of the deposited a-SiCN:H thin films, as determined by combined RBS and ERDA analyses. The films are Si-rich carbonitrides containing 32–52 at.% Si, 16–44 at.% N, and a relatively small carbon fraction of 3–5 at.%. The hydrogen concentration varies within a narrow range of 25–30 at.%. The precursor gas flow ratios, deposition rates, and resulting film thicknesses are summarized in Table 1.

Fig. 2 illustrates the dependence of the elemental ratios C/Si and N/Si on the corresponding precursor gas ratios. The C/Si ratio exhibits a linear relationship with the CH_4/SiH_4 flow ratio, described by the fitting function $y = 0.174 \cdot x$, where x denotes the gas flow ratio. In contrast, the N/Si ratio as a function of NH_3/SiH_4 shows a strong nonlinearity for $x < 1$, corresponding to the regime where N-doped a-Si:H is formed and nitrogen incorporation is more efficient [31]. In this range, the data were fitted using a power-law function $y = 0.527 \cdot x^{0.54}$. At higher x values, the dependence becomes approximately linear and can be expressed as $y = 0.265 + 0.27 \cdot x$. It should be noted that silane acts as the host precursor because its Si–H bonds (318 kJ/mol) dissociate more readily under plasma conditions than the C–H bonds in CH_4 (411 kJ/mol) or the N–H bonds in NH_3 (386 kJ/mol) [32]. As a result, the slopes of the linear-region fitting curves remain below unity.

Fig. 3 presents the AFM images and cross-sectional topography of the a-SiCN:H films. All samples exhibited uniform and smooth surfaces. The observed surface morphology, characterized by the absence of noticeable clusters or grains, is typical of amorphous thin films. The surface roughness, quantified by the root mean square (R_q) and arithmetic mean (R_a) values, is summarized in Table 1. Both R_q and R_a depend on film thickness as well as on the applied deposition parameters. Similar to sample 4, which exhibits R_a = 0.46 nm, a mean roughness of approximately 0.4 nm has been reported for a 600 nm-thick C-rich a-SiCN:H layer deposited by PECVD using SiH_4, CH_4, and N_2 gas precursors [9]. Comparable roughness values have also been reported for a-SiNC coatings synthesized from various disilazane precursors using the rf-PECVD technique [10].

The uniform and smooth surface morphology observed in the present PECVD-grown a-SiCN:H films can be attributed to the ion-assisted growth mechanism inherent to plasma-enhanced deposition. During the initial stages of growth, a high nucleation density promotes rapid coalescence of islands into a continuous amorphous network. Simultaneously, energetic ion bombardment enhances species mobility, enabling surface relaxation and densification that suppress columnar or granular evolution. This ion-assisted surface diffusion mechanism has been extensively discussed for PECVD-grown a-SiN and a-SiCN films, where increased ion flux, moderate substrate heating, and appropriate precursor selection yield dense, featureless surfaces with sub-nanometer roughness [33]. The low RMS roughness values obtained in this work thus indicate that the growth regime is dominated by ion-assisted

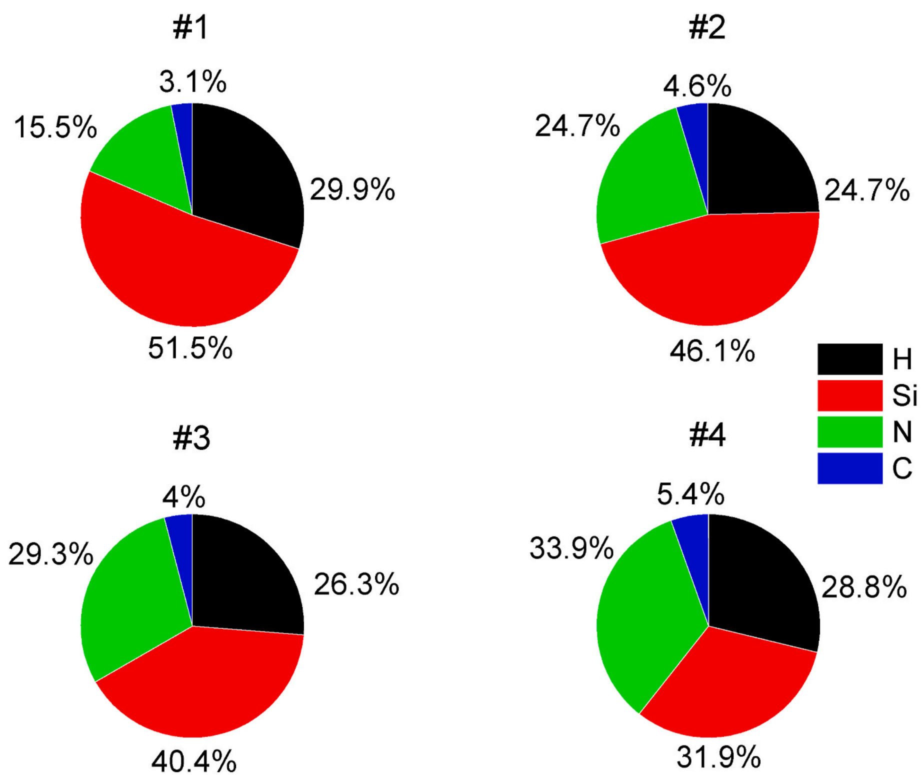

Fig. 1. Elemental composition of the a-SiCN:H thin films.

Table 1
Sample list, precursor gas flows, growth rates, film thickness, and RMS (R_q) and mean (R_a) roughness.

Sample	SiH_4 SCCM	CH_4 SCCM	NH_3 SCCM	H_2 SCCM	Growth rate, Å/s	Thickness, nm	R_q, pm	R_a, pm
1	4.0	1.4	1.4	36.0	3.0	717	874	691
2	3.7	1.9	3.8	33.7	3.4	407	655	520
3	3.5	2.3	5.8	31.4	3.7	684	742	581
4	3.1	3.0	9.2	27.8	4.0	627	623	462

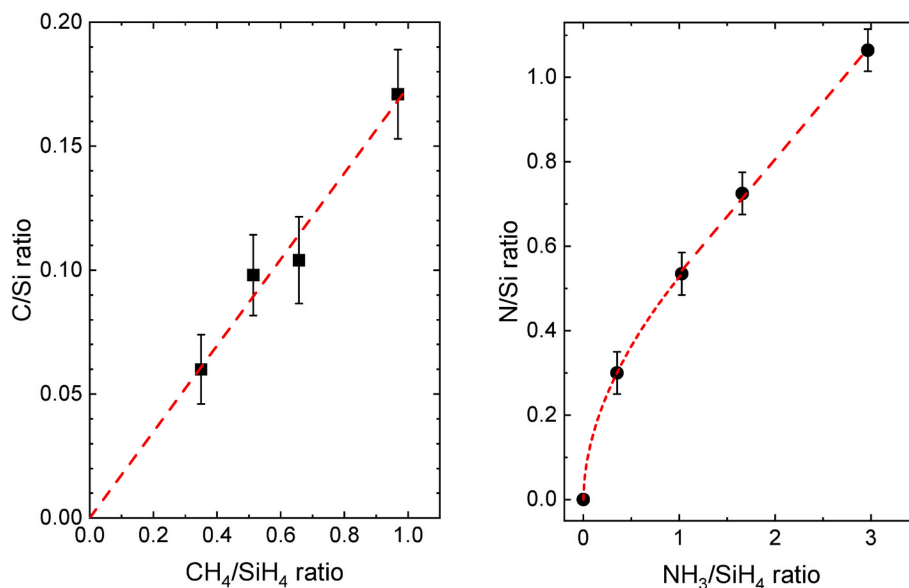

Fig. 2. Elemental concentration ratios versus precursor gas flow ratios: (a) C/Si vs. CH_4/SiH_4, and N/Si vs. NH_3/SiH_4.

surface relaxation rather than shadowing or porous growth, leading to compact and defect-free amorphous structures.

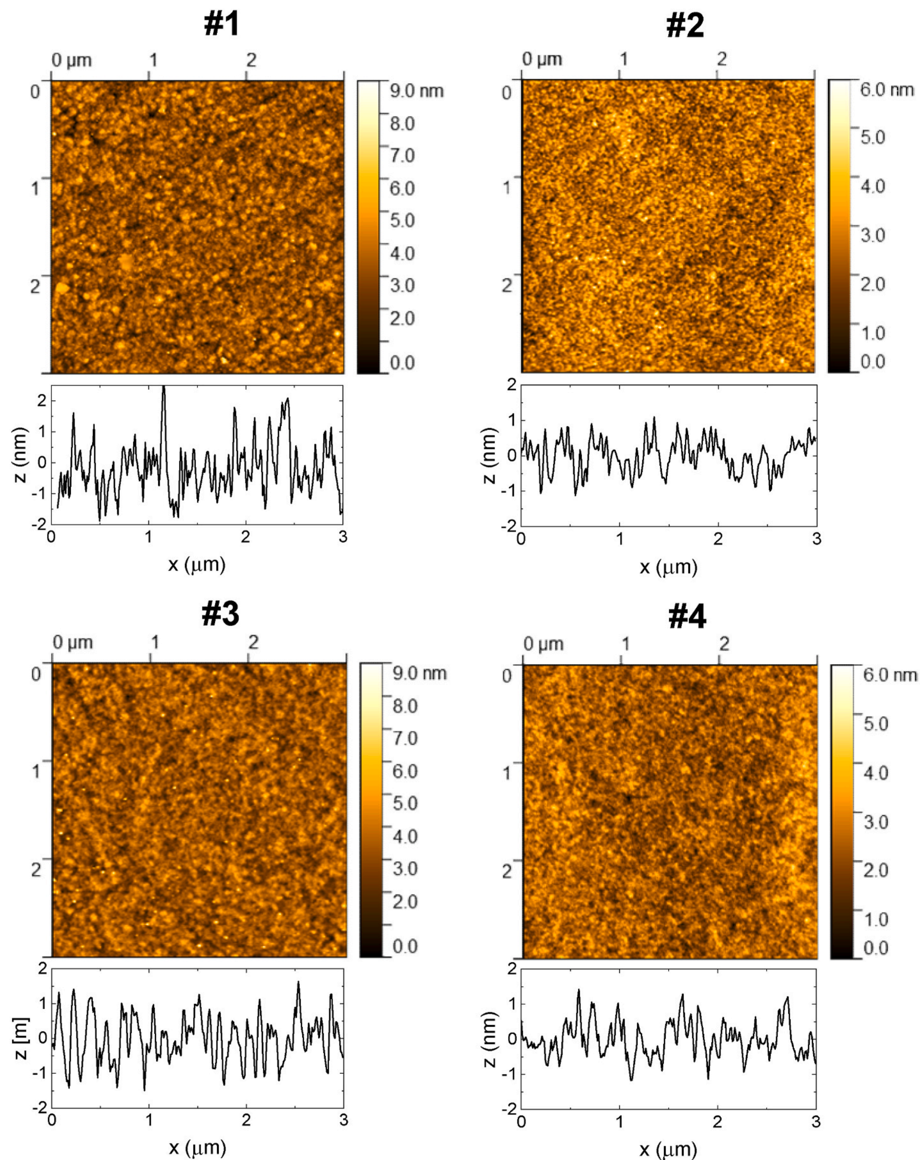

Fig. 3. Two-dimensional atomic force microscopic images and cross-sectional profiles of a-SiCN:H thin films.

The precise determination of optical constants from transmittance spectra is highly sensitive to the surface quality of thin films. Even slight surface irregularities can induce additional light scattering and diffuse transmission, thereby reducing the measured transmittance and distorting interference fringes, which introduces uncertainties in spectra modeling. The smooth and homogeneous morphology of the present a-SiCN:H films ensures well-defined interference patterns and minimizes optical losses associated with surface scattering. Accordingly, the low roughness values confirmed by AFM measurements indicate that the films possess the necessary surface quality for accurate and reliable determination of optical constants from their transmittance spectra.

4.2. Dielectric functions

Fig. 4 shows the experimental and calculated transmission spectra of the a-SiCN:H thin-films. In the transparent region, the amplitude of the interference fringes increases slightly with rising photon energy, which is attributed to an increasing refractive index. However, the fringes begin to diminish in the Urbach tail region and disappear entirely in the fundamental absorption region. The best fit for the spectra was achieved using a polynomial order of 3. The fitted model parameters are provided in Table 2. The parameter E_g, which ranges from 2.26 to 2.87eV, is lower than 3.59 eV value reported for stoichiometric silicon nitride deposited under similar conditions [26]. This suggests that the optical properties of a-SiCN:H are closer to those of Si-rich nitrides [34], due to the limited carbon content ($\leq$6 % at.%).

Using the fitted model parameters, the optical dielectric function and its sub-gap components were calculated for each sample. Fig. 5a and b presents the real part of the dielectric function, $\varepsilon_1(E)$, and its sub-gap contribution, $\varepsilon_{1,sg}(E)$, respectively. The extrapolated zero-energy value of $\varepsilon_1(E)$ decreases from approximately 5 to 3.5 as the optical bandgap increases, accompanied by a shift of the main peak toward higher photon energies. The amplitude of the $\varepsilon_{1,sg}(E)$ component is about two orders of magnitude lower than that of $\varepsilon_1(E)$, indicating that the near-band-edge absorption represented by $\varepsilon_{2,sg}(E)$ contributes only weakly to $\varepsilon_1(E)$ through the Kramers–Kronig relation.

Fig. 6a shows the imaginary part of the dielectric function, $\varepsilon_2(E)$, plotted on a semi-logarithmic scale, indicating the energy parameters E_g and E_c. The ε_2 value at 5 eV decreases by a factor of 9 as E_g increases from 2.26 to 2.87 eV. The Urbach tail region ($E < E_c$) deviates from a simple exponential dependence, suggesting that the band-edge absorption cannot be accurately described by conventional dispersion models [23,

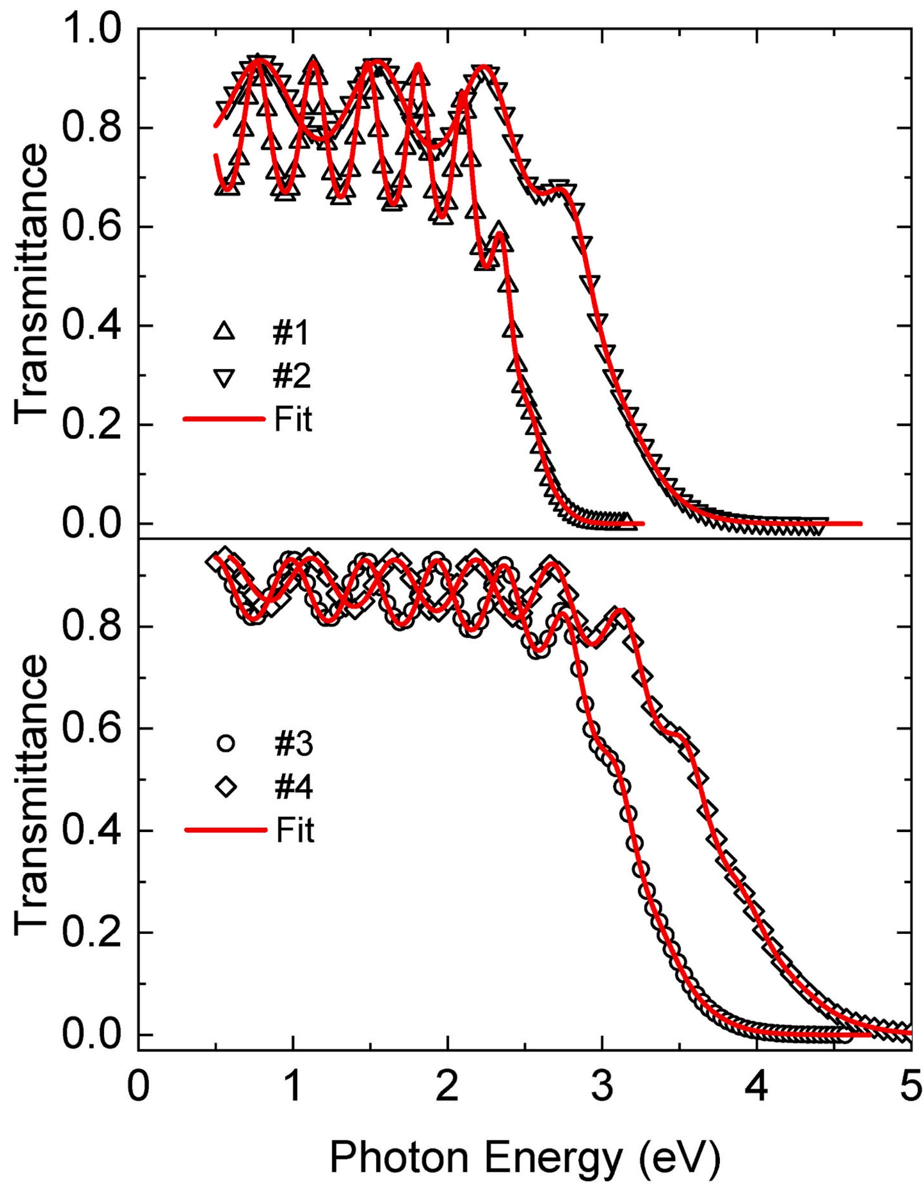

Fig. 4. Experimental (symbols) and simulated (lines) transmission spectra of the a-SiCN:H thin-films.

Table 2
Fitted parameters of the XTL model for the a-SiCN:H films.

Sample N	E_g, eV	E_o, eV	C, eV	A, eV	E_c, eV	b_1	b_2	b_3
1	2.255	4.401	4.768	130.4	2.957	6.341	−16.53	36.71
2	2.539	6.105	8.324	95.03	3.359	5.921	−15.39	28.68
3	2.683	7.636	8.72	75.17	3.414	7.472	−12.71	47.74
4	2.868	8.622	5.047	56.49	3.699	7.556	−3.598	61.03

24].

Fig. 6b shows the $\varepsilon_{2,sg}(E)$ curves, representing absorption bands with peaks at energies exceeding the respective bandgaps. These curves are asymmetric: the low-energy tail forms a sub-linear trend in a semi-logarithmic plot at $E < E_g$ (as shown in Fig. 6a), while the high-energy tail is steeper and approaches zero as E nears E_c. In the range $E_g < E < E_c$, $\varepsilon_{2,sg}(E)$ is expressed as the difference between the $\varepsilon_{2,X}(E)$ and $\varepsilon_{2,TL}(E)$ (see Eq. (3)), making it dependent on Tauc-Lorentz oscillator parameters, E_c, and polynomial coefficients. When assuming exponential band tails, band-edge absorption has been analyzed using the joint density-of-states (JDOS) function, where the parameter γ denotes the transition point between square-root and exponential state distributions, thus offering a quantitative measure of the amorphous network disorder [35]. In the XTL model, $\gamma = E_c - E_g$ holds an equivalent significance according Eq. (1a), where

$$\varepsilon_{2,TL}(E_c) = \frac{\gamma^2 A E_0 C}{\left(E_c^2 - E_0^2\right)^2 + C^2 E_c^2} \cdot \frac{1}{E_c} \ . \tag{12}$$

Although γ varies within a narrow range of 0.7–0.83 eV, the magnitude of the absorption band decreases by a factor of 10 as the bandgap increases. This reduction is driven by changes in the parameters A, C, and E_0, resulting in reduced fundamental absorption. The XTL

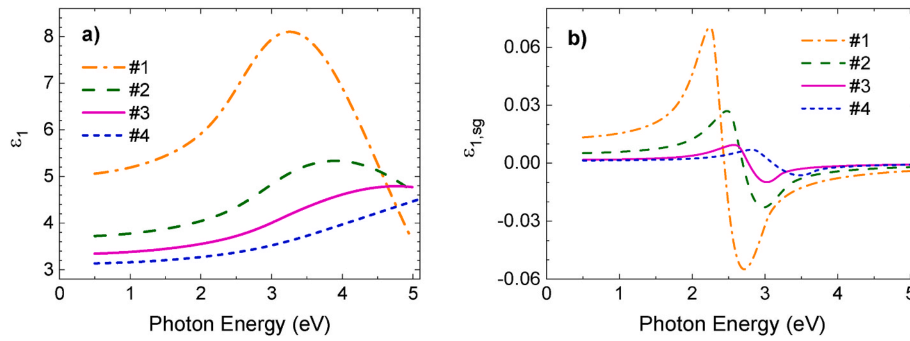

Fig. 5. (a) Real part of the dielectric function and (b) its sub-gap component.

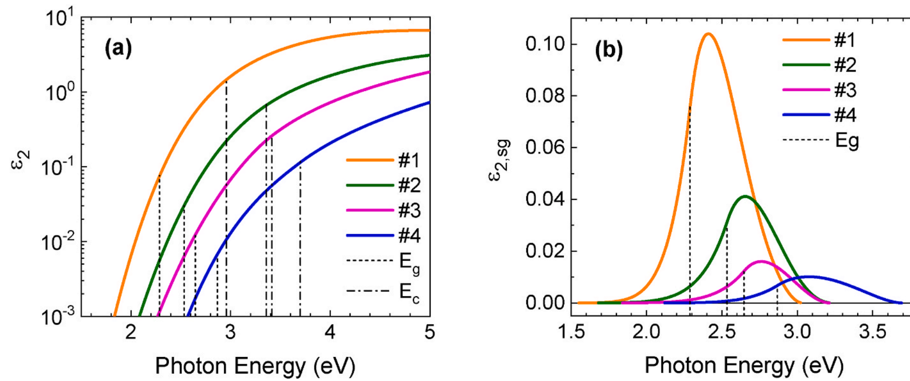

Fig. 6. (a) Imaginary part of the dielectric function and (b) its sub-gap component. The XTL model parameters E_g and E_c are represented by the dashed lines.

model, therefore, provides a detailed analysis of the band-edge absorption and can be used for estimating the degree of disorder in semiconductor or dielectric materials.

4.3. Optical bandgap and optical constants

The optical bandgaps were determined from Tauc plots, as shown in Fig. 7. The Tauc optical gap, E_{op}, was obtained by fitting the linear region of the $E\sqrt{\varepsilon_2}$ versus E dependence and extrapolating the fitted line to intersect the energy axis at $y = 0$. The extracted E_{op} values were then correlated with the elemental N/Si ratio, as illustrated in Fig. 8. The resulting dependence is nearly linear and can be expressed as $E_{op}=1.89 + 1.414 \cdot x$, where x denotes the N/Si ratio. The extrapolated value at $x = 0$ corresponds well to the optical bandgap range 1.8–2 eV previously reported for a-$Si_{1-x}C_x$:H films deposited from hydrogen-diluted silane–-methane plasma [36]. The observed increase in E_{op} with nitrogen incorporation reflects the progressive widening of the bandgap due to enhanced Si–N bond formation and reduced density of localized states near the band edges, consistent with the transition toward a more insulating amorphous SiCN network [31].

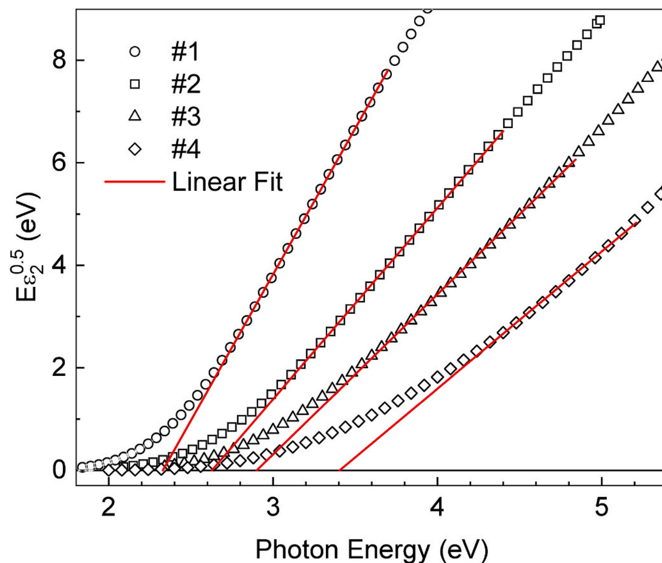

Fig. 7. Tauc plot. The optical band gap is determined from the intercept of the extrapolated fitted line with the energy axis.

Fig. 9 presents three-dimensional surface plots of the refractive index

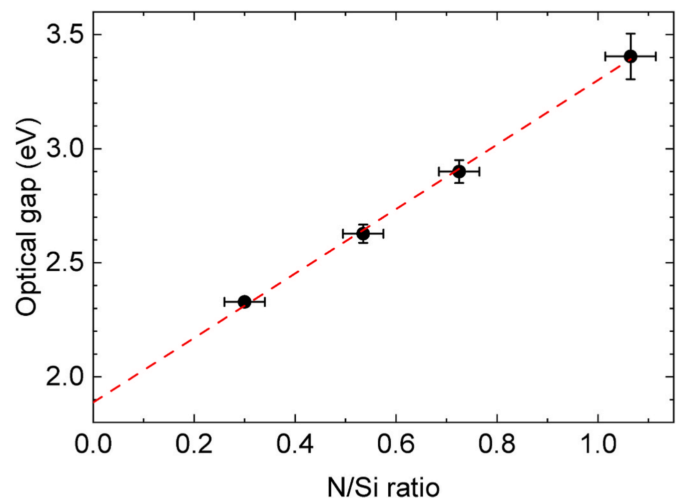

Fig. 8. Variation of the optical bandgap (E_{op}) as a function of the elemental N/Si ratio in the a-SiCN:H thin films.

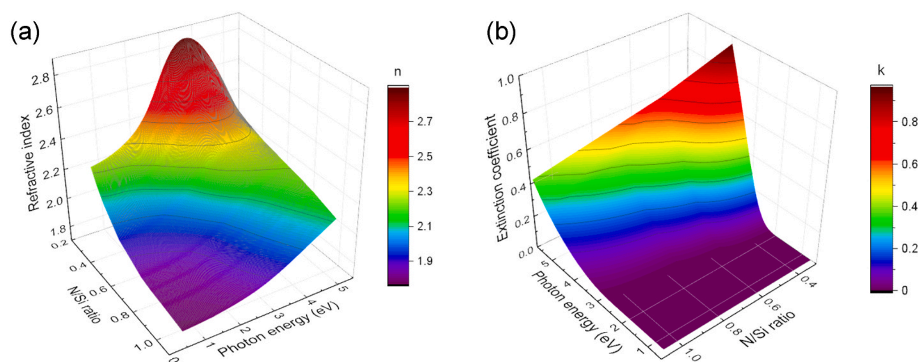

Fig. 9. (a) Refractive index and (b) extinction coefficient as a function of the photon energy and elemental N/Si ratio in the a-SiCN:H thin films.

(n) and extinction coefficient (k) dispersion data as a function of photon energy and the elemental N/Si ratio in the a-SiCN:H thin films. The refractive index varies from 1.77 to 2.9, exhibiting a maximum at an Si/N ratio of 0.3 and a photon energy of approximately 3.5 eV. In contrast, the k-plot displays a monotonic, gently sloping topology. In the spectral range corresponding to the fundamental absorption edge, the extinction coefficient decreases progressively with increasing Si/N ratio at a fixed photon energy. As a result, the spectral region in which $k \approx 0$ becomes broader and shifts toward the blue. This reduction in absorption therefore directly reflects a compositional shift of the optical transparency window from longer wavelengths (red) to shorter wavelengths (blue). At the telecommunication wavelength of 1550 nm, the refractive index decreases gradually from 2.26 to 1.79 as the Si/N ratio increases from 0.3 to 1.0. These results demonstrate that compositional adjustment of the Si/N ratio enables precise control over the optical constants of a-SiCN:H films, highlighting their potential for tailored optoelectronic and photonic applications across visible and near-infrared spectral ranges.

5. Conclusions

Hydrogenated amorphous silicon carbonitride thin films were successfully synthesized by rf-PECVD at low temperature with controlled composition through adjustment of precursor gas flow ratios. RBS/ERDA analysis confirmed Si-rich films with limited carbon incorporation and stable hydrogen content. AFM measurements revealed atomically smooth surfaces, ensuring high reliability in optical characterization. Spectral fitting using the XTL model accurately reproduced the measured transmittance spectra and provided a physically consistent description of the dielectric function, including sub-gap absorption features. The optical bandgap increased nearly linearly with the N/Si ratio, indicating band widening associated with Si–N bond formation and reduced disorder. The refractive index exhibited a strong compositional dependence, varying from 1.77 to 2.9 across the measured spectral range. These findings confirm that rf-PECVD is a highly versatile technique for the low-temperature growth of a-SiCN:H films with tunable optical properties, making them promising candidates for applications in antireflective coatings, optical filters, and integrated photonic devices.

CRediT authorship contribution statement

Y. Vygranenko: Writing – review & editing, Writing – original draft, Visualization, Software, Methodology, Data curation, Conceptualization. **G. Lavareda:** Writing – review & editing, Writing – original draft, Investigation, Data curation, Conceptualization. **A. Amaral:** Supervision, Resources, Project administration, Formal analysis. **P. Brogueira:** Supervision, Resources, Project administration, Funding acquisition.

Declaration of competing interest

The authors declare that they have no known competing financial interests or personal relationships that could have appeared to influence the work reported in this paper.

Acknowledgements

This work was supported by FCT under Grant UID/04540, CeFEMA, Centre of Physics, Engineering and Advanced Materials and under Grant UIDB/00066, CTS, Centre of Technology and Systems.

Data availability

Data will be made available on request.

References

[1] Z. Khatami, P.J. Simpson, P. Mascher, Process-dependent mechanical and optical properties of nanostructured silicon carbonitride thin films, Nanotechnology 30 (2019) 314003, https://doi.org/10.1088/1361-6528/ab180c.
[2] A.M. Wrobel, P. Uznanski, Hard silicon carbonitride thin-film coatings by remote hydrogen plasma chemical vapor deposition using aminosilane and silazane precursors. 2: physical, optical, and mechanical properties of deposited films, Plasma Process. Polym. 18 (2021) e2000241, https://doi.org/10.1002/ppap.202000241.
[3] D. Li, S. Guruvenket, M. Azzi, J.A. Szpunar, J.E. Klemberg-Sapieha, L. Martinu, Corrosion and tribo-corrosion behavior of a-SiC$_x$:H, a-SiN$_x$:H and a-SiC$_x$N$_y$:H coatings on SS301 substrate, Surf. Coating. Technol. 204 (2010) 1616–1622, https://doi.org/10.1016/j.surfcoat.2009.10.018.
[4] C. Huber, B. Stein, H. Kalt, Plasma-enhanced chemical vapor deposition of amorphous silicon carbonitride: deposition temperature dependence of bonding structure, refractive index, mechanical stress and their aging under ambient air, Thin Solid Films 634 (2017) 66–72, https://doi.org/10.1016/j.tsf.2017.05.004.
[5] S. Bulou, L. Brizoual, P. Miska, L. Poucques, J. Bougdira, M. Belmahi, Wide variations of sicxny:h thin films optical constants deposited by H_2/N_2/Ar/hexamethyldisilazane microwave plasma, Surf. Coating. Technol. 208 (2012) 46–50, https://doi.org/10.1016/j.surfcoat.2012.07.079.
[6] A. Bachar, A. Bousquet, H. Mehdi, G. Monier, C. Robert-Goumet, L. Thomas, M. Belmahi, A. Goullet, T. Sauvage, E. Tomasella, Composition and optical properties tunability of hydrogenated silicon carbonitride thin films deposited by reactive magnetron sputtering, Appl. Surf. Sci. 444 (2018) 293–302, https://doi.org/10.1016/j.apsusc.2018.03.040.
[7] G. Lavareda, Y. Vygranenko, A. Amaral, C. Nunes de Carvalho, N.P. Barradas, E. Alves, P. Brogueira, Dependence of optical properties on composition of silicon carbonitride thin films deposited at low temperature by PECVD, J. Non-Cryst. Solids 551 (2021) 120434, https://doi.org/10.1016/j.jnoncrysol.2020.120434.
[8] J.A. Silva, S. Quoizola, E. Hernandez, L. Thomas, F. Massines, Silicon carbon nitride films as passivation and antireflective coatings for silicon solar cells, Surf. Coating. Technol. 242 (2014) 157–163, https://doi.org/10.1016/j.surfcoat.2014.01.037.
[9] B. Sha, A.N. Lukianov, M.G. Dusheiko, V.B. Lozinskii, A.N. Klyui, D.V. Korbutya, S. E. Pritchin, N.I. Klyui, Carbon-rich amorphous silicon carbide and silicon carbonitride films for silicon-based photoelectric devices and optical elements: application from UV to mid-IR spectral range, Opt. Mater. 106 (2020) 109959, https://doi.org/10.1016/j.optmat.2020.109959.
[10] A. Sobczyk-Guzenda, K. Oleśko, M. Gazicki-Lipman, W. Szymański, J. Balcerzak, B. Wendler, H. Szymanowski, Chemical structure and optical properties of a-SiNC coatings synthesized from different disilazane precursors with the RF plasma

enhanced CVD technique - a comparative study, Mater. Res. Express 6 (2019) 016410, https://doi.org/10.1088/2053-1591/aae4f9.
[11] A. Frigg, A. Boes, G. Ren, I. Abdo, D.-Y. Choi, S. Gees, A. Mitchell, Low loss CMOS-compatible silicon nitride photonics utilizing reactive sputtered thin films, Opt. Express 27 (26) (2019) 37795–37805, https://doi.org/10.1364/OE.380758.
[12] C.-H. Cheng, C.-S. Fu, H.-Y. Wang, S.Y. Set, S. Yamashita, G.-R. Lin, Review on optical nonlinearity of group-IV semiconducting materials for all-optical processing, APL Photon 7 (2022) 081101, https://doi.org/10.1063/5.0102342.
[13] T. Berlind, N. Hellgren, M.P. Johansson, L. Hultman, Microstructure, mechanical properties, and wetting behavior of Si-C-N thin films grown by reactive magnetron sputtering, Surf. Coating. Technol. 141 (2001) 145–155, https://doi.org/10.1016/S0257-8972(01)01236-1.
[14] Q. Li, C. Chen, M. Wang, Y. Lv, Y. Mao, M. Xu, Y. Wang, X. Wang, Z. Zhang, S. Wang, W. Zhao, Study on photoelectricity properties of SiCN thin films prepared by magnetron sputtering, J. Mater. Res. Technol. 15 (2021) 460–467, https://doi.org/10.1016/j.jmrt.2021.08.043.
[15] V.S. Sulyaeva, A.N. Kolodin, M.N. Khomyakov, A.K. Kozhevnikov, M.L. Kosinova, Enhanced wettability, hardness, and tunable optical properties of SiC_xN_y coatings formed by reactive magnetron sputtering, Materials 16 (4) (2023) 1467, https://doi.org/10.3390/ma16041467.
[16] N.-M. Park, S.H. Kim, G.Y. Sung, Band gap engineering of SiCN film grown by pulsed laser deposition, J. Appl. Phys. 94 (2003) 2725–2728, https://doi.org/10.1063/1.1594267.
[17] I. Tanaka, S. Matuoka, Y. Harada, Mechanical properties of amorphous SiCN films deposited by ion-beam-assisted deposition, Diam. Relat. Mater. 121 (2022) 108732, https://doi.org/10.1016/j.diamond.2021.108732.
[18] L. Beliaev, E. Shkondin, A. Lavrinenko, O. Takayama, Optical, structural and composition properties of silicon nitride films deposited by reactive radio-frequency sputtering, low pressure and plasma-enhanced chemical vapor deposition, Thin Solid Films 763 (2022) 139568, https://doi.org/10.1016/j.tsf.2022.139568.
[19] B.P. Swain, N.M. Hwang, Study of structural and electronic environments of hydrogenated amorphous silicon carbonitride (a-SiCN:H) films deposited by hot wire chemical vapor deposition, Appl. Surf. Sci. 254 (2008) 5319–5322, https://doi.org/10.1016/j.apsusc.2008.02.077.
[20] Md M. Rahman, S.K. Hasan, Ellipsometric, XPS and FTIR study on SiCN films deposited by hot-wire chemical vapor deposition method, Mater. Sci. Semicond. Process. 42 (2016) 373–377, https://doi.org/10.1016/j.mssp.2015.11.006.
[21] A.O. Kozak, V.I. Ivashchenko, O.K. Porada, L.A. Ivashchenko, T.V. Tomila, V. S. Manjara, G.V. Klishevych, Structural, optoelectronic and mechanical properties of PECVD Si-C-N films: an effect of substrate bias, Mater. Sci. Semicond. Process. 88 (2018) 65–72, https://doi.org/10.1016/j.mssp.2018.07.023.
[22] A. Abdelal, Z. Khatami, P. Mascher, A comparative study of a-SiCN:H thin films fabricated with acetylene and methane, ECS J. Solid State Sci. Technol. 12 (2023) 013002, https://doi.org/10.1149/2162-8777/aca9fb.
[23] S. Ferlauto, G.M. Ferreira, J.M. Pearce, C.R. Wronski, R.W. Collins, Analytical model for the optical functions of amorphous semiconductors from the near-infrared to ultraviolet: applications in thin film photovoltaics, J. Appl. Phys. 92 (2002) 2424–2436, https://doi.org/10.1063/1.1497462.
[24] L.V. Rodríguez-De Marcos, J.I. Larruquert, Analytic optical-constant model derived from Tauc-lorentz and Urbach tail, Opt. Express 24 (2016) 28561–28572, https://doi.org/10.1364/OE.24.028561.
[25] G. Lavareda, Y. Vygranenko, A. Amaral, P. Brogueira, Effect of dehydrogenation on optical constants of silicon nitride thin films, Opt. Mater. 145 (2023) 114480, https://doi.org/10.1016/j.optmat.2023.114480.
[26] Y. Vygranenko, G. Lavareda, Extended Tauc-Lorentz model for amorphous materials with non-exponential band tails, IEEE Electron Device Lett. 45 (2024) 2146–2149, https://doi.org/10.1109/LED.2024.3458392.
[27] G.E. Jellison Jr., F.A. Modine, Parameterization of the optical functions of amorphous materials in the interband region, Appl. Phys. Lett. 69 (1996) 371–373, https://doi.org/10.1063/1.118064.
[28] K. Ohta, H. Ishida, Comparison among several numerical integration methods for kramers-kronig transformation, Appl. Spectrosc. 42 (1988) 952–957, https://doi.org/10.1366/0003702884430380.
[29] R.T. Phillips, A numerical method for determining the complex refractive index from reflectance and transmittance of supported thin films, J. Phys. D Appl. Phys. 16 (1983) 489–497, https://doi.org/10.1088/0022-3727/16/4/010.
[30] L. Vriens, W. Rippens, Optical constants of absorbing thin solid films on a substrate, Appl. Opt. 22 (1983) 4105–4110, https://doi.org/10.1364/AO.22.004105.
[31] P. Temple-Boyer, L. Jalabert, L. Masarotto, J.L. Alay, J.R. Morante, Properties of nitrogen doped silicon films deposited by low-pressure chemical vapor deposition from silane and ammonia, J. Vac. Sci. Technol. A 18 (5) (2000) 2389–2393, https://doi.org/10.1116/1.1286714.
[32] T.L. Cottrell, The Strengths of Chemical Bonds, second ed., 1965, p. 502. Butterworths, London, 1958, p. 270; B. deB. Darwent, "National standard reference data series," National bureau of standards, No. 31, Washington, DC, 1970; S.W. Benson, J. Chem. Educ 42.
[33] A. Sinibaldi, E. Descrovi, F. Giorgis, L.T. Karabacak, Y.P. Zhao, G.C. Wang, T.M. Lu, Growth front roughening in silicon nitride films by plasma-enhanced chemical vapor deposition, Phys. Rev. B 66 (7) (2002) 075329, https://doi.org/10.1103/PhysRevB.66.075329.
[34] D.T.H. Tan, K.J.A. Ooi, D.K.T. Ng, Nonlinear optics on silicon-rich nitride - a high nonlinear figure of merit CMOS platform, Photon, Res 6 (2018) 50–66, https://doi.org/10.1364/PRJ.6.000B50.
[35] S.K. O'Leary, S.R. Johnson, P.K. Lim, The relationship between the distribution of electronic states and the optical absorption spectrum of an amorphous semiconductor: an empirical analysis, J. Appl. Phys. 82 (7) (1997) 3334–3340, https://doi.org/10.1016/S0257-8972(01)01236-1.
[36] Y. Vygranenko, M. Fernandes, P. Louro, M. Vieira, A. Sazonov, Optoelectronic properties of a-$Si_{1-x}C_x$:H films grown in hydrogen diluted silane-methane plasma, Phys. Status Solidi 7 (3) (2010) 782–785, https://doi.org/10.1002/pssc.200982779.